

J-CAMD 255

Nucleotide-binding properties of adenylate kinase from *Escherichia coli*: A molecular dynamics study in aqueous and vacuum environments*

Petra Kern^a, Roger M. Brunne^{b,**} and Gerd Folkers^{a,***}

^aDepartment of Pharmacy, ETH, Winterthurerstrasse 190, CH-8057 Zürich, Switzerland

^bDepartment of Physical Chemistry, ETH-Hönggerberg, CH-8092 Zürich, Switzerland

Received 24 January 1994

Accepted 31 March 1994

Key words: GROMOS; Domain movement; Phosphate transfer

SUMMARY

The complex of adenylate kinase with its transition-state inhibitor has been studied by molecular dynamics simulations in water and in vacuum environments with the GROMOS force field over a period of 300 ps. The adenylate kinase, a member of the nucleotide-binding protein family, was exemplarily chosen for the inspection of the nucleotide-binding properties in the active site. The ligand binding and the domain movements have been studied in detail over the simulation period and compared with the crystal structure. Secondary structure transitions and domain closures defined those parts of the structure which are involved in an induced-fit movement of the enzyme. The presence of more stable hydrogen bonds on the substrate side leads to the assumption that substrate binding is more specific than cosubstrate binding. Reliable results were achieved only if water was explicitly included in the simulation.

INTRODUCTION

The nucleotide-binding protein family comprises a wide range of proteins with different functions. Comparisons of their folding pattern and secondary structure elements have been described in the literature [1,2]. One reason for the great interest in nucleotide-binding properties is the possible application in modern virus or cancer therapy. Antimetabolites of the nucleoside type are used as anticancer drugs. Their use results in disruption of nucleic acid synthesis, either by inhibiting key enzymes in this process or by altering cellular function following incorporation into RNA or DNA. Since a high selectivity of these antimetabolites for one enzyme is required, it is important to study the interaction complexes between the protein and the antimetabolite at the atomic level.

*Dedicated to Prof. Dr. J. Seydel on the occasion of his 65th birthday.

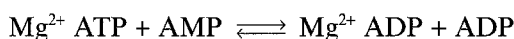
**Present address: Bayer AG, Pharma Research Centre, D-42096 Wuppertal, Germany.

***To whom correspondence should be addressed.

The thymidine kinase encoded by herpes simplex virus type 1 (HSV1-TK) is a target enzyme for antiviral therapy with nucleoside analogs [3]. The difference in substrate specificity between cellular and virus-induced TK serves as the basis for the selectivity of antiviral nucleoside analogs. Since the TK is also involved in DNA metabolism and cell proliferation [4], knowledge of the TK structure might lead to the development of efficient drugs against herpes infections and those cancer types which are associated with increased TK levels or TK oncogene products.

A 3D model of the thymidine kinase structure is based on homology modeling with adenylate kinase. Therefore, the study of the nucleotide-binding properties was exemplarily done with adenylate kinase [5]. The results may subsequently be transferred to thymidine kinase.

Adenylate kinases are small monomeric enzymes that catalyze the transfer of a phosphate group from ATP to AMP. The comparison of their known primary sequences [6] shows a pairwise homology of around 30%. Most of the enzymes of the ADK family transfer the phosphate group according to the following equation:



The variability of the accepted cosubstrates is much higher than that of the substrates. For example, the enzyme of the mitochondrial matrix, AK3, uses Mg^{2+} GTP instead of Mg^{2+} ATP [7].

Several crystal structures of the ADK family have been solved, either as a complex between the protein and a substrate or cosubstrate, or as an isolated protein. Some controversy exists regarding the assignment of substrate and cosubstrate location, because none of the described complexes were solved with both substrate and cosubstrate in the active site [8,9]. A breakthrough has come from the crystal structure of the ADK of *Escherichia coli* [10], in complex with the inhibitor P₁,P₅-bis-(adenosine-5')-pentaphosphate (Ap₅A), mimicking both substrate and cosubstrate positions. Fitting the backbone atoms of this complex to those of other nucleotide-binding proteins such as AK3, guanylate kinase or H *ras*-p21 allowed the assignment of the ATP and AMP positions [7,11]. Ap₅A fixes the enzyme in a transition state in which the additional fifth phosphate group connects ATP to AMP.

In general, the ADK family is separated into two classes of short and long ADKs, depending on the absence or presence of an additional insertion domain. In the adenylate kinase obtained from *E. coli*, the insertion is located between residues Val¹²¹ and Asp¹⁵⁹ (Fig. 1). This extra domain consists of a four-stranded β -sheet, connected with short loops; it is involved in an induced-fit movement [12]. The stability of this domain is compared to the main structure, which appears to be similar in all ADKs. A subdivision of the enzyme into three domains (main, insertion and AMP-binding domain) has been described by Müller and Schulz [10]. The main domain consists of different structural elements, e.g. a central β -sheet and a phosphate-binding loop, which are common in all nucleotide-binding proteins.

The aim of this study is to analyze the dynamic properties of the ADK-inhibitor complex in both water and vacuum environment, using the MD simulation method. A study of the rearrangement and the relative mobility of the different domains is part of this investigation. Further-

Abbreviations: ADK, adenylate kinase; ATP, adenosine-5'-triphosphate; AMP, adenosine-5'-monophosphate; Ap₅A, P₁,P₅-bis-(adenosine-5')-pentaphosphate; MD, molecular dynamics; GMP, guanosine-5'-monophosphate; GTP, guanosine-5'-triphosphate; AK3, adenylate kinase from the mitochondrial matrix; AK_{eco}, adenylate kinase from *Escherichia coli*; Ef-Tu, elongation factor Tu; H *ras*-p21, human *ras*-p21; PFK, phosphofructokinase.

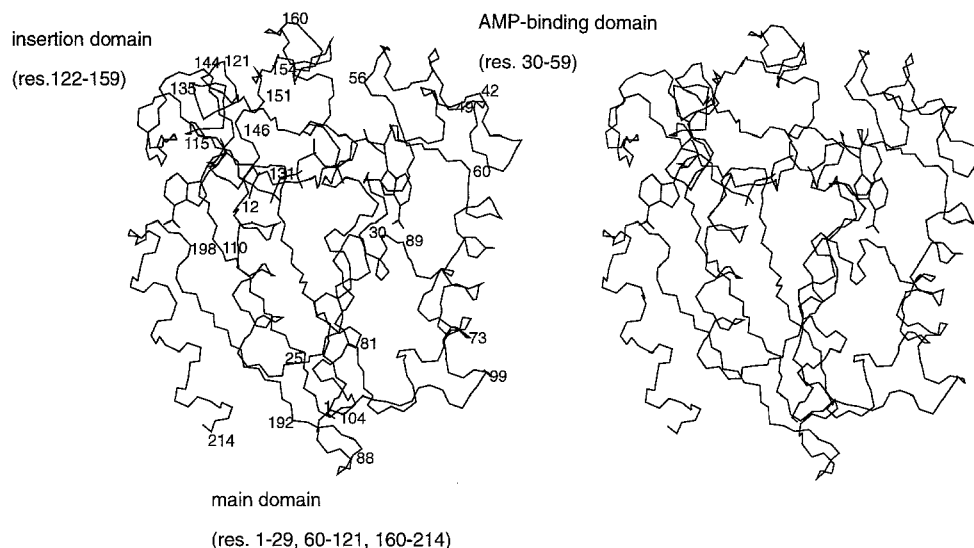


Fig. 1. The backbone of the *Akeco* structure, including the transition-state inhibitor Ap_5A . Three different domains and several residues mentioned in the text are marked.

more, the MD simulation provides dynamic information at the atomic level, which helps to explain experimental observations such as the discrimination of AMP from GMP and the ability of the enzyme to accept another cosubstrate instead of ATP [13]. Those residues which are supposed to be involved in the catalysis have been investigated more thoroughly. The physical properties of the bound inhibitor and its geometry in the active site are described in detail.

MATERIALS AND METHODS

Computational methods

Molecular mechanics and dynamics simulations were performed using the GROMOS87 program library [14]. Simulations with explicit inclusion of water molecules were run on the NEC SX-3/22 computer of the Centro Svizzero di Calcolo Scientifico in Manno, Ticino, Switzerland, whereas the *in vacuo* simulations were done on an IBM RISC 6000 workstation at the ETH Zürich. Graphics display and analysis of the trajectories were achieved with the SYBYL 6.0 molecular modeling package [15], implemented on an ESV workstation.

Preparation of the input coordinates

The initial structure for the solvent and *in vacuo* simulations was taken from X-ray data [10] of the complex between the adenylate kinase and its inhibitor Ap_5A , solved at 0.19 nm resolution. Two different crystal structures, with a C^α rms deviation of 0.037 nm between them, were present in the data file. The complex I, including conformation A of the additional phosphate and the Arg^{167} residue, was chosen as the input structure because of the better quality of its electron density map. All water molecules were removed from the input, with the exception of one internal water molecule, located near the Ap_5A active site. The system contained 2097 atoms (214 residues and Ap_5A) and three additional atoms from the water molecule.

Water simulation

The GROMOS united-atom force field was used for the enzyme–substrate complex. For the water molecules the SPC/E model [16] was chosen. Polar hydrogens were treated explicitly. Arginine and lysine amino acids were protonated and aspartic acid and glutamic acid residues were negatively charged, in agreement with physiological conditions at pH 7. The total charge of the complex added up to $-9\ e^-$, including the $-5\ e^-$ at the inhibitor part of the complex. Initial strain in the unsolvated complex was removed by 100 steps of steepest descent and 100 steps of conjugate gradient energy minimization. During the latter stage, bond lengths were kept constant using the SHAKE algorithm [17]. For the water simulation the minimized complex was embedded into an octahedral box of equilibrated SPC/E water, with a maximum solute–solvent overlap of 0.23 nm and a minimum solute–wall distance of 0.85 nm. The resulting box had a volume of 178 nm³ and contained 4937 water molecules with a total of 16 908 atoms.

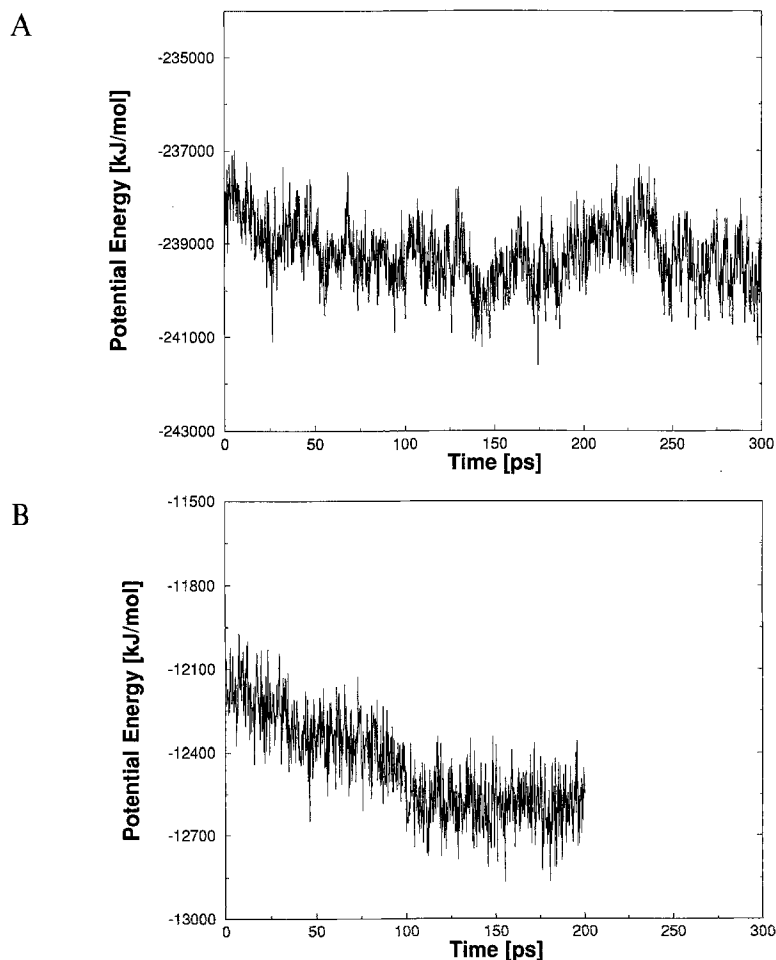


Fig. 2. Total potential energy as a function of time of (A) the 300 ps water simulation and (B) the 200 ps vacuum simulation.

The system was equilibrated in several stages. After an initial 20 steps of steepest descent energy minimization, with harmonical positional constraints on the whole complex in order to adjust the solute–water interaction, the whole system was minimized for another 100 steps without any positional restraining. Nonbonded interactions were calculated within a cutoff of 0.8 nm. These energy-minimized coordinates were then used as starting point for the molecular dynamics simulation.

Initial atomic velocities were taken from a Maxwellian distribution at $T = 300$ K. The system was coupled to a heat bath at 300 K, with separate scaling of the protein and solvent molecules [18]. The temperature coupling constant was 0.01 ps and the pressure coupling constant 0.05 ps for the first 2 ps; these parameters were set afterwards to 0.1 and 0.5 ps, respectively. All bond lengths were constrained at their equilibrium values with a geometrical tolerance of 10^{-4} nm using the SHAKE algorithm, which allows a simulation time step of 2 fs to be used. The nonbonded interactions were calculated within a short-range cutoff radius of 0.8 nm and a long-range cutoff radius of 1.2 nm for charge interactions, without the use of switching functions. The latter were only calculated every 10 steps, when the nonbonded pair list was updated. After 10 ps of initial equilibration, the time origin was reset to 0 and the MD simulation was continued for a period of 300 ps.

For analysis, the coordinates were stored every 25 steps (0.05 ps). Energy values were saved every 50 steps (0.1 ps). The simulation was separately averaged and analyzed over two periods of 100 ps length, ranging between 100–200 ps and 200–300 ps, respectively.

Vacuum simulation

The GROMOS87 RT37d4 parameter set was used and a zero net charge on all residues and the inhibitor was maintained. One internal water molecule near the active site was included. The in vacuo simulation started from the same energy-minimized structure used as input for the MD water simulation. After additional 600 steps steepest descent energy minimization, using SHAKE and a cutoff radius of 0.8 nm, the MD simulation was started for a period of 210 ps. The non-bonded cutoff was 0.8 nm for short-range interactions and 1.0 nm for long-range charge interactions. Averaging and analysis of the complex was done over the last 100 ps.

RESULTS AND DISCUSSION

Time dependence of ADK properties

The total potential energy as a function of time is illustrated in Fig. 2 for the water and the in vacuo simulations. All sampled conformations during the 300 ps MD study are energetically more favourable than the energy-minimized starting structure (not shown). In the water simulation, the potential energy fluctuates with small deviations around a mean value. For the in vacuo simulation the total energy drops for the first 100 ps, until it reaches a stable value around which it fluctuates.

The magnitude of the radius of gyration in the in vacuo simulation is 7.6% smaller than in the solvated case, consistent with the contraction of proteins in vacuum simulations due to protein–vacuum boundary effects [19]. The water simulation yielded a structure much more similar to the crystal structure than that derived from the in vacuo simulation. In the case of the water simulation, the rms deviation of the conformation with respect to the initial crystal structure after energy minimization and 10 ps MD simulation was 0.147 nm for all atoms and 0.105 nm for the C^α atoms (Fig. 3). The rms deviations for C^α and all atoms slowly increased over the simulation period.

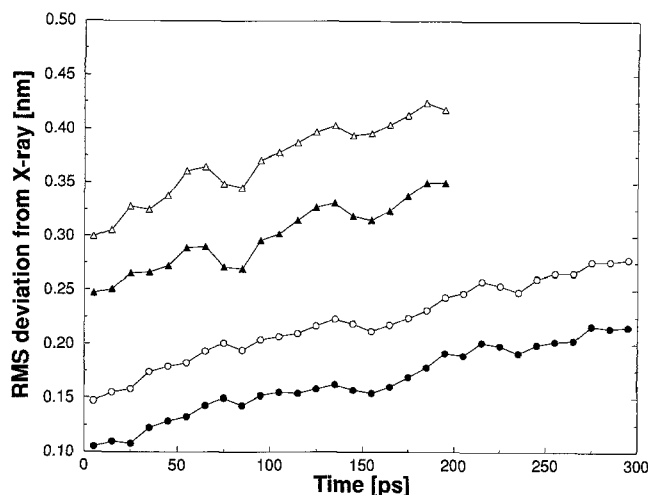


Fig. 3. Variation of the rms displacement of the atom positions, averaged over 10 ps subtrajectories relative to the crystal structure. The water and in vacuo simulations are indicated by circles and triangles, respectively. The filled symbols represent the results obtained for the C^α atoms, the open symbols those for all atoms.

In order to determine whether the increase of the rms values was caused by particular parts of the protein, rms deviations were calculated for different segments (Fig. 4). As large fluctuations and rms deviations were seen for the insertion domain (residues 120–159), the C^α atoms of the remaining part of the structure (residues 1–117 and 160–214) were chosen as a reference for the comparison. These residues appeared to be equilibrated after 50 ps, with an asymptotic value of 0.15 nm. The increase after 170 ps, which was caused by a movement and distortion within the insertion domain (residues 120–159), is reduced but still observable. Several dihedral angle transitions occurred around this time. Some sections within the reduced set show considerably

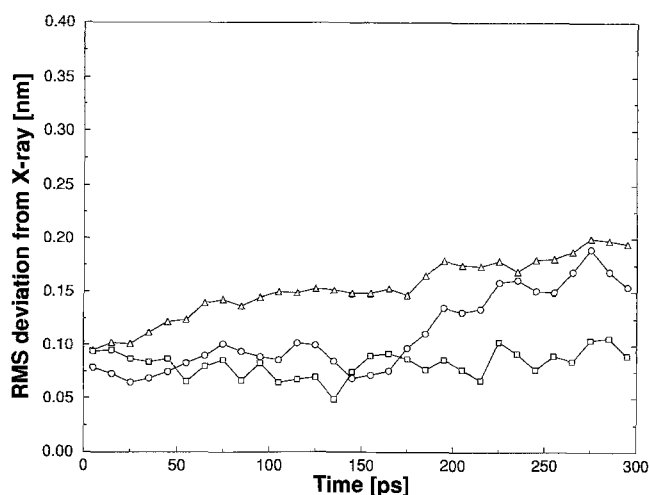


Fig. 4. The rms displacement of the C^α atoms of selected parts of the structure relative to the crystal structure. Triangles, circles and squares denote respectively the whole structure without the insertion domain (residues 1–117, 160–214), the phosphate-binding loop (residues 1–44) and helix 2 (residues 30–42).

less deviation from the crystal structure. For instance, helix 2 (residues 30–42) retains its crystal conformation, with an rms deviation of 0.06 nm (100–200 ps) or 0.08 nm (200–300 ps) for the MD water simulation (Table 1). The phosphate-binding loop exhibits a behaviour similar to the whole structure, because its rms deviation still increases at the end of the simulation period. A more detailed analysis of three structures, time-averaged over 160–170, 170–180 and 180–190 ps of the water simulation, was carried out to determine the reason for the sharp increase of rms values around 170 ps. Apart from the very flexible insertion domain, the deviations were caused by dihedral angle transitions within the pentapeptidic section Val¹¹⁷-Val¹²¹, located before the insertion domain.

Parallel curves, still increasing at 200 ps and shifted to much higher values, can be observed for the *in vacuo* simulation. Due to slower energy exchange it would be necessary to simulate over a longer period in order to obtain full equilibration [19].

Positional deviation of ADK from the crystal structure

Representative MD structures for comparison were obtained by averaging the atomic coordinates over periods of 100 ps length; 100–200 and 200–300 ps for the water simulation and

TABLE 1
POSITIONAL RMS DEVIATION FROM THE CRYSTAL STRUCTURE FOR ADK ATOMS

Section	Residues	rms1 (nm)		rms2 (nm)	
		100–200 ps	200–300 ps	100–200 ps	200–300 ps
All C ^α atoms		0.154		0.197	
Main domain	1–29, 60–121, 160–214	0.155	0.150	0.187	0.177
Insertion domain	122–159	0.186	0.117	0.268	0.156
AMP-binding domain	30–59	0.096	0.092	0.122	0.113
Phosphate-binding loop	1–44	0.082	0.055	0.153	0.079
α-Helices					
1	12–25	0.079	0.038	0.182	0.051
2	30–42	0.064	0.058	0.082	0.055
3	49–56	0.102	0.081	0.176	0.140
4	60–73	0.120	0.038	0.098	0.054
5	89–99	0.160	0.110	0.150	0.129
6	115–121	0.117	0.052	0.317	0.112
7	160–188	0.159	0.139	0.210	0.191
8	210–214	0.306	0.239	0.296	0.199
β-Strands					
1	1–6	0.081	0.056	0.090	0.060
2	27–29	0.066	0.042	0.169	0.078
3	81–84	0.101	0.099	0.137	0.124
4	104–110	0.096	0.067	0.117	0.074
5	122–126	0.063	0.061	0.159	0.067
6	131–135	0.152	0.081	0.253	0.058
7	144–146	0.167	0.146	0.260	0.382
8	151–154	0.087	0.074	0.082	0.074
9	192–198	0.161	0.118	0.142	0.121

Coordinates of the ADK of the water simulation were time averaged over 100–200 and 200–300 ps and compared with the crystal structure. Deviations in nanometers have been calculated for the C^α atoms, after fitting the whole structure (rms1) or selected sections (rms2).

100–200 ps for the in vacuo simulation. The averaged structures obtained from the water simulation are almost identical to the crystal structure, whereas the averaged structure from the in vacuo simulation exhibits greater deviations, characterized by a net contraction of the structure in the absence of solvent forces (Figs. 5A and B, respectively). The rms deviations of the C $^{\alpha}$ atoms from the crystal structure are 0.154 nm (100–200 ps) and 0.197 nm (200–300 ps) for the water structures, and 0.319 nm for the in vacuo structure, respectively. These numbers are comparable with those from MD simulations of similar systems [20,21], where the vacuum boundary condition caused large structural deviations as well. Therefore, we limit the analysis in the rest of this section to the water simulation.

Residues with positional deviation values larger than the average are located at the C-terminus (residues 200–214) and at the surface of the protein, where they are involved in intermolecular crystal contacts (residues 44–48, 74–78, 141–152 and 173–180).

A secondary structure analysis of the crystal structure and both averaged structures of the water simulation was performed using the DSSP program by Kabsch and Sander [22]. The comparison of both secondary structure assignments (by Schulz et al. [10] and our DSSP calculation) for the crystal structure yielded the same result. The α -helices are remarkably similar in the

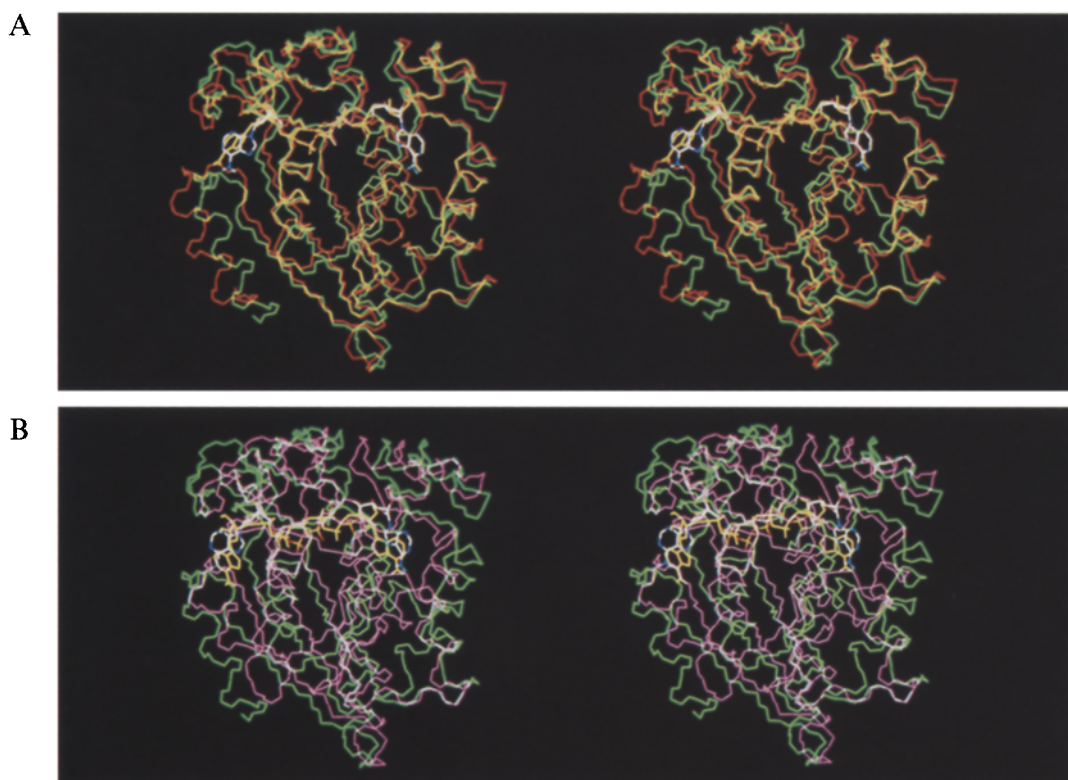


Fig. 5. Stereoview of the superimposition of the crystal structure (protein backbone: green; Ap₅A: type-coded) and the MD time-averaged conformation (100–200 ps) of (A) the water simulation (protein backbone: red; Ap₅A: yellow) and (B) the in vacuo simulation (protein backbone: violet; Ap₅A: yellow).

crystal structure and in both water simulation mean structures. The α -helices 7 and 8 of the crystal structure, which are separated by only one amino acid, fused together into one helix during the simulation period. Residues 144–147 and 151–154, which are labelled as β -strands in the crystal structure [10], are not identified as regular secondary structure motifs of the MD structures by the DSSP program. Additionally, a difference between the crystal and the MD averaged structures occurs for helix 6. In the structure averaged over 200–300 ps, helix 6 ranges from residue 113 to 119. It is shifted by two residues (115–121) compared to the crystal structure. In our further analysis, helices 7 and 8 of the crystal structure are combined and are labelled as helix 7; helix 9 will be renamed to helix 8.

The positional deviations for various domains and individual sections corresponding to secondary structure elements indicate whether some parts have been modified more than others. These deviations are reported in Table 1 (Fig. 1). The general folding of the protein structure is well preserved in the water simulation, whereas strong distortions occur if the water solvent is neglected.

The deviations of the individual sections after fitting to all C^α atoms of the crystal structure (rms1 in Table 1) are mostly smaller than the deviation of all C^α atoms, which indicates large deviations for the irregular sections. The C-terminal helices 7 and 8 lie at the surface of the enzyme and helix 6 belongs to the insertion domain, thus explaining the higher rms1 values for these sections in the structures averaged over 200–300 ps. All of these sections are not directly involved in the binding of the inhibitor. The insertion domain comprising residues 122–159 is more affected than the other domains. It is involved in the induced-fit movement during the catalysis reaction, hence a higher rms deviation value corresponds to the expected flexibility of this domain. The outer β -strand 7, fully exposed to the solvent in the insertion domain, undergoes conformational changes, explaining the large rms1 value of the whole domain. The central β -sheet (ranging from β -strand 1 to β -strands 4 and 9), which is a common structural motif of nucleotide-binding proteins [23], is accurately reproduced. Most of the significant deviations occur in irregular structure elements, such as loops and turns.

Separate positional fits over the C^α atoms of each structural domain (insert, main, AMP-binding and the phosphate-binding loop) and secondary structure sections were performed in order to determine to what extent rigid-body movement of the substructures or conformational changes within the sections contribute to the positional deviations. A highly decreased rms2 value (Table 1) compared to that of the global fit indicates that the domain or the secondary structure segment was only rotated or translated with respect to the crystal structure. Calculating the rms1 for the insertion domain in this way, the value decreased from 0.186 to 0.117 nm (100–200 ps) and from 0.268 to 0.156 nm (200–300 ps). β -strand 6 (131–135), as part of this domain, changed

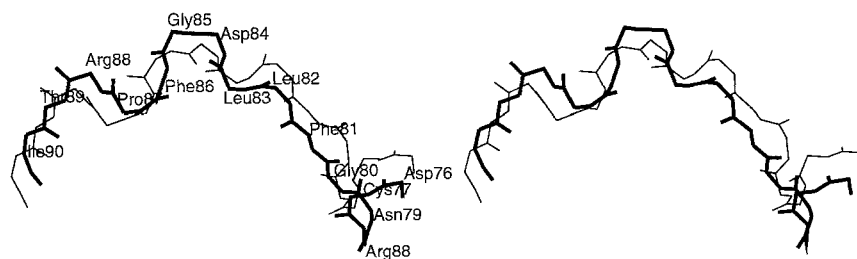


Fig. 6. Superimposition of residues 76–90 of the crystal structure (thick line) and the 100–200 ps water MD time-averaged structure (thin line) to indicate backbone modifications for this section.

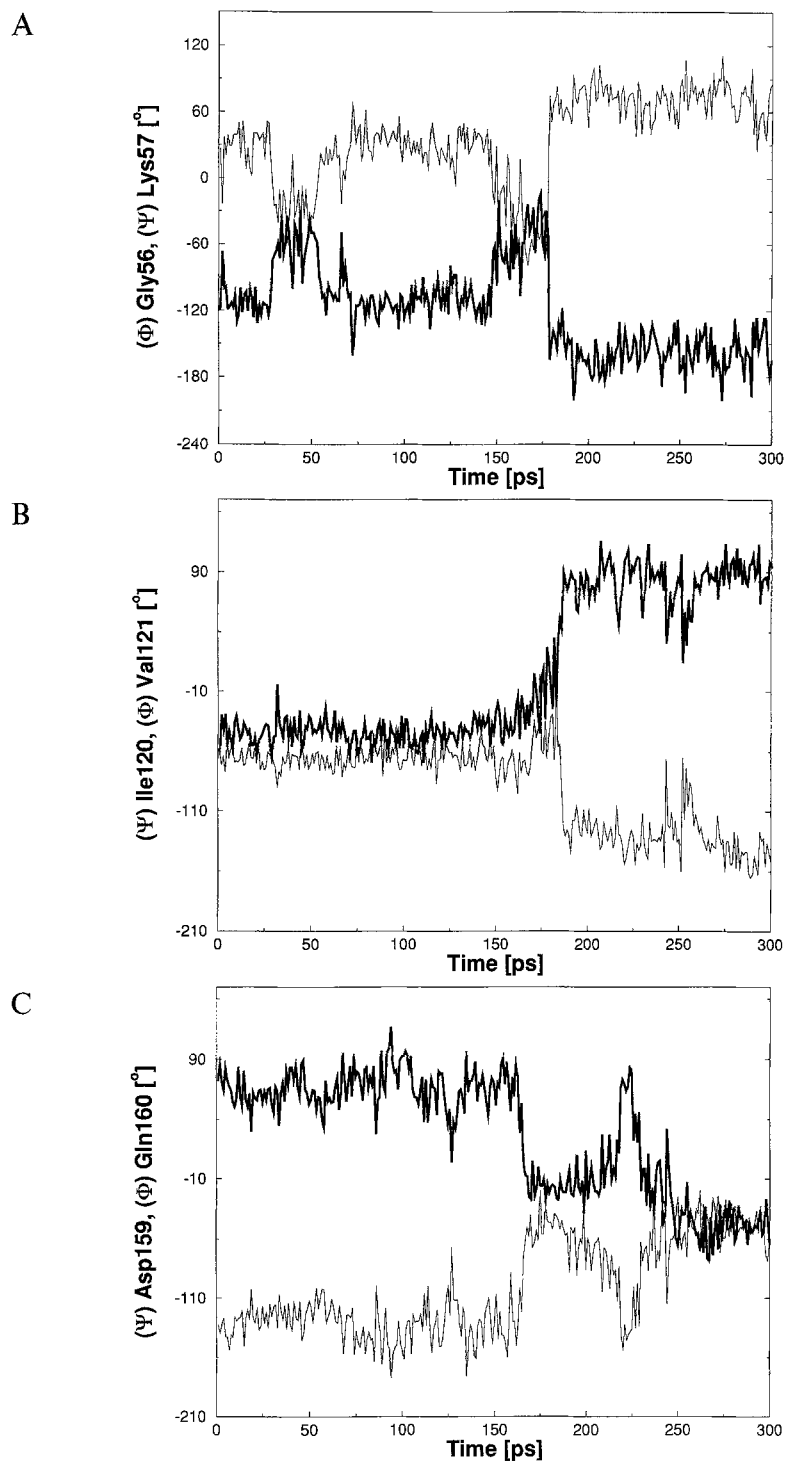


Fig. 7. Variations of the backbone dihedral angle of selected residues with time. The ψ angles are represented by the thin line and the ϕ angles by the thick line.

its location due to a rigid-body motion and helix 6, located in front of the insertion domain, moved as a rigid body and caused the insertion domain to move closer to the main domain. The main-domain helices 1, 4 and 8 and β -strand 9 showed small rigid-body motions.

Dihedral angle deviation of ADK from the crystal structure

Backbone modifications between the crystal structure and the 100–200 ps MD structure were localized by calculation of the ϕ and ψ angles of all adenylate kinase residues. More than 80% of the ϕ, ψ dihedral angle deviations do not exceed 30° , with the exception of some irregular structures which showed variations up to 100° . This is observed for several residues situated in loops and turns. ψ of residues 79 and 85 and ϕ of residues 80, 86 and 189 (Fig. 6), which all belong to residues in loops and turns of the main domain, show a deviation from their values in the crystal structure of more than 60° . A deviation of similar size is found for the dihedral angles ψ in resi-

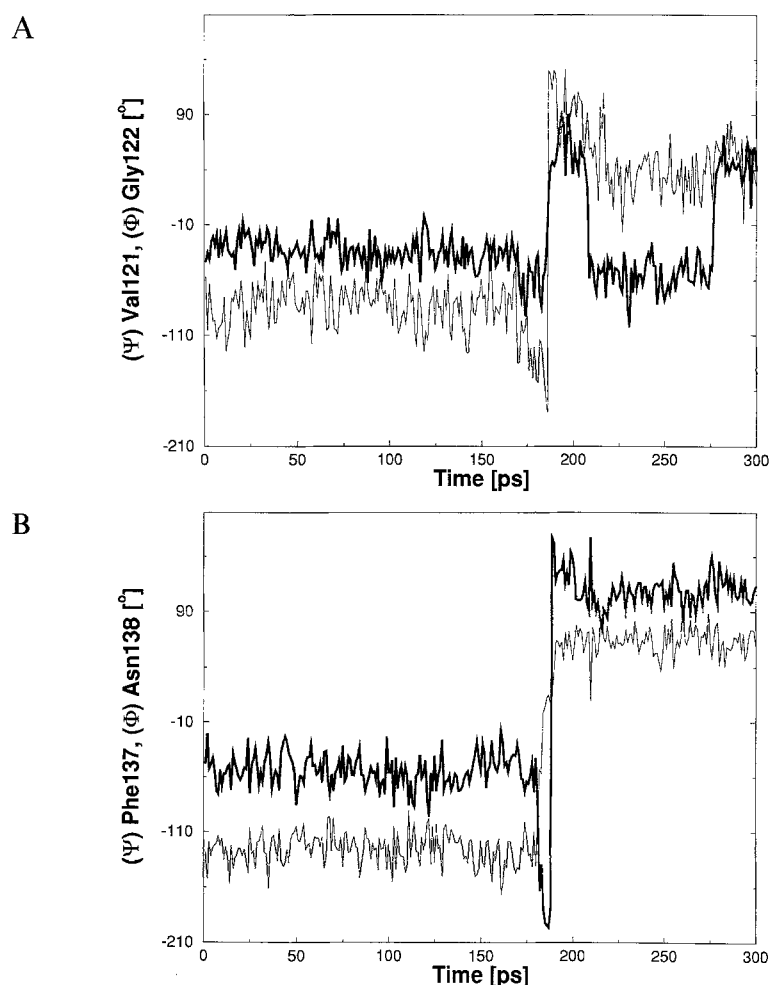


Fig. 8. Variations of the backbone dihedral angles ψ of Val¹²¹ and ϕ of Ile¹²² (A) and ψ of Phe¹³⁷ and ϕ of Asn¹³⁸ (B) with time (ψ : thin line; ϕ : thick line).

dues 129, 130, 137 and 149 and ϕ in residues 131, 138 and 150 in the insertion domain. The rms fluctuation of the dihedral angles ψ in residues 56, 120, 121, 122, 137, 149, 150, 159 and 189 and ϕ in residues 46, 57, 122, 138, 150, 151, 160 and 190 from the trajectory average is also increased to values larger than 30° , which indicates the occurrence of different dihedral angle conformations during the simulation period. Time series of these dihedral angles with large rms fluctuations were inspected for transitions (Figs. 7A–C). Nearly all ψ -angle transitions of residues 56, 120, 149 and 159 are corrected by the consecutive ϕ -angle movement, corresponding with a rotation of the plane of the peptide bond. These transitions occur around 170 ps, thus explaining the increase in the positional rms deviation value of the C^α atoms around this time step. Transitions of ψ angles of residues 137 and 121 at 170 ps are not corrected by the consecutive dihedral angle, so that the conformational changes near these residues influence the entire structure (Figs. 8A and B).

The induced-fit movement of ADK has been described [24] and four sections have been proposed which are responsible for the movement of the domains. These sections are mobile regions at which torsional angle transitions occur, influencing the whole structure. The dihedral angle ψ of residue 115, responsible for the first region, does not show significant movement or distortion during the simulation. The deviation from the value in the crystal structure is only 10° . The deformation of the second region is caused by ψ of residues 121 and 122 and ϕ of residue 122, which is a shift of one amino acid compared to the proposal of Gerstein et al. (Fig. 9) [24]. Torsion angles ψ of residues 154, 155 and 174, responsible for the third and fourth mobile region, remain at stable values over the trajectory. However, our MD simulation reveals that the third and fourth sections can be combined. Transitions of the dihedral angles around residues 158–160 are responsible for the reorientation of one hinge involved in the domain closure (Fig. 10). Additionally, transitions for $\psi(137)$ and $\phi(138)$ were observed during the simulation. Residues Phe¹³⁷ and Asn¹³⁸ are located in the turn after β -strand 6 in the insertion domain and are involved in the stabilization of the ATP–adenine complex (Fig. 11). Deformations caused by the mobility of the regions take place at the N- and C-termini of helices 6 and 7, which connect the flexible insertion domain with the rest of the protein.

Asp¹⁵⁸ and Asp¹⁵⁹ are highly conserved residues in the ADK family [6]. Moreover, their negatively charged carboxylate groups interact with the positively charged guanidinium moieties of Arg¹⁵⁶ and Arg¹²³, which are involved in stabilization of the inhibitor phosphate groups. A transition of $\phi(158)$ and $\psi(159)$ at 170 ps coincides with the observed AMP α -phosphate movement at this time. The main backbone fold is preserved, whereas the orientation of the Asp¹⁵⁸ and Asp¹⁵⁹ side chains changes considerably (Fig. 10). The movement of the Asp¹⁵⁹ side chain influ-

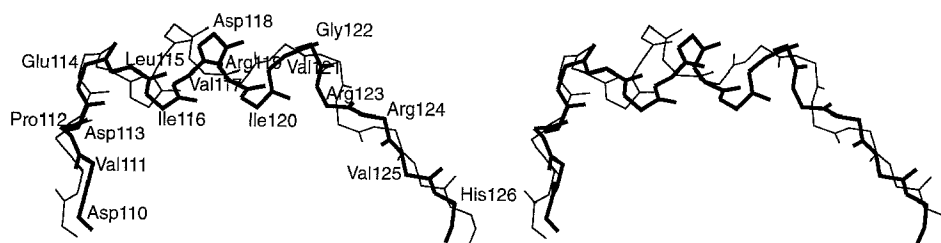


Fig. 9. Superimposition of residues 110–126 of the crystal structure (thick line) and the 100–200 ps water MD time-averaged structure (thin line), demonstrating the variations of the backbone dihedral angle involved in the second joint of the induced-fit movement of ADK.

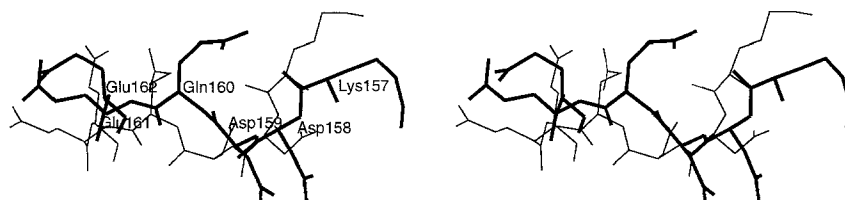


Fig. 10. Superimposition of residues 157–162 of the crystal structure (thick line) and the water MD time-averaged structure (thin line), including also the side-chain atoms for inspection of the Asp¹⁵⁸ and Asp¹⁵⁹ movement.

ences the conformation of Arg¹²³ and weakens the hydrogen bonding from Arg¹²³ towards the ATP γ -phosphate and to the additional phosphate group. Because of the side-chain movement of Asp¹⁵⁸, the salt bridge between Asp¹⁵⁸ and Arg¹⁵⁶ breaks and the guanidinium group then points away from the α -phosphate. The loss of a hydrogen bond increases the flexibility of the α -phosphate. Another example of dihedral angle transitions that cause side-chain reorganizations is found for Phe¹³⁷ and Asn¹³⁸. Phe¹³⁷ is located in an irregular structure of the insertion domain and is involved in ATP binding at the same time.

Rms deviation of Ap₅A from the crystal structure

The simulation of the complex in a water environment gives a good account of the crystal structure with respect to both protein structure and inhibitor. Substrate and cosubstrate have similar positions as in the crystal structure. In particular the side of the inhibitor mimicking the AMP site exhibits small deviations from the crystal structure. The base moiety of the ATP is rotated, as can be seen from the large deviation values of the adenine atoms. Rotation of this adenine ring is followed by shifts of side chains of the surrounding residues Phe¹³⁸ and Arg¹¹⁹, parallel towards the ring. Both base moieties of the inhibitor rotate and translate when solvent

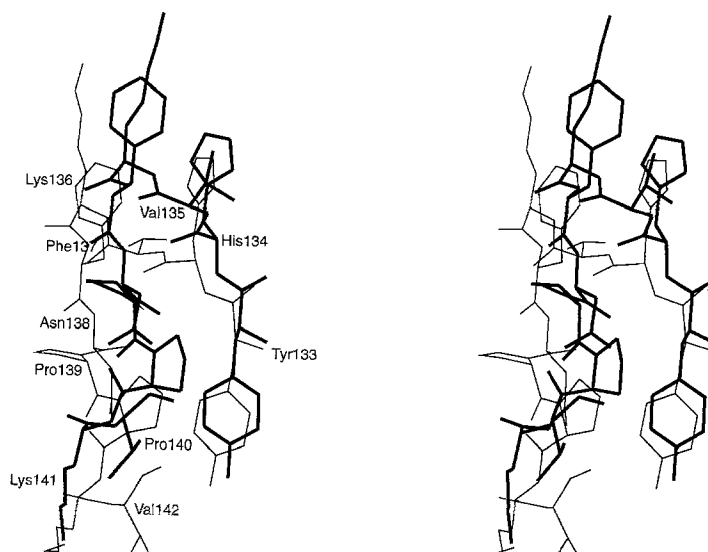


Fig. 11. Superimposition of residues 133–142 of the crystal structure (thick line) and the 100–200 ps water MD time-averaged structure (thin line), including also the side-chain atoms.

molecules are omitted in the simulation. The γ -phosphate atoms, which would be transferred during the catalysis reaction, show deviations between 0.19 and 0.24 nm.

The phosphate transfer reaction requires the exclusion of water from the active site. In the crystal structure, 13.4 nm² out of the 61.1 nm² of the maximum solvent-accessible surface area of Ap₅A are exposed to water. During the MD simulation the water-accessible surface of Ap₅A increases from 16.8 nm² after 200 ps to 24.1 nm² after 300 ps, out of the maximum solvent-accessible surface area of 63 nm². The ATP adenine, all five phosphate groups and the AMP ribose are exposed to the water molecules. Only the ATP ribose and the AMP adenine are buried by surrounding residues. Considering the individual parts of Ap₅A, we observe that the solvent-accessible surface area increases for all parts, with the exception of the ATP β -phosphate, the AMP adenine and the additional connecting phosphate group. The AMP adenine remains buried in its pocket, which agrees with the specific binding data for adenine at this site [25]. The additional fifth phosphate group, which connects the AMP and ATP parts of Ap₅A, is almost completely buried, rather than the γ -phosphate which was expected to be excluded from water [10]. The crystalline water molecule, which was included in the MD simulation, leaves its position near the γ -phosphate shortly after 10 ps, but it is replaced by various other water molecules throughout the simulation. Two water molecules are permanently hydrogen-bonded to the oxygens of the γ -phosphate group. The increase of the water accessibility at the AMP α -phosphate coincides with the loss of hydrogen bonds connecting residue Arg¹⁵⁶ and the α -phosphate after 120 ps.

Atomic positional fluctuations

The positional rms fluctuations of all C $^{\alpha}$ atoms were calculated from the 100–200 ps trajectories of the water and in vacuo simulations and are displayed in Fig. 12. The positional fluctuations are largest for the in vacuo simulation, with the exception of the N-terminal part. Positional fluctuations of the C $^{\alpha}$ atoms in the crystal structure were calculated from the crystallographic B-factors and are included in Fig. 12 for comparison with the atomic fluctuations of the MD simulation. Residues with large fluctuations in the crystal also move significantly in the simulation. The curves derived from the crystal structure and the water simulation data have nearly the same shape, but the values from the water simulation are 30–50% smaller throughout. As was already seen from the positional rms deviations from the crystal structure, residues with large fluctuations are located in loops, turns, and at the beginning or end of the insertion domain. None of these mobile residues is involved in the binding of the inhibitor.

Positional fluctuations of side-chain atoms, represented by C $^{\gamma}$ atoms, are larger than 0.15 nm only in loops at the outer parts of the protein. Some residues around the inhibitor show significant side-chain shifts, followed by a modified binding of the inhibitor. The aromatic side chains of His¹³⁴ and Phe¹³⁷ rotate and affect the binding properties of the inhibitor. The rotation of the ATP adenine part coincides with a parallel arrangement of the side chains of Phe¹³⁷ and Arg¹¹⁹, both forming a ‘sandwich complex’ with the adenine moiety.

The atomic positional fluctuation of the inhibitor Ap₅A is presented in Fig. 13. The inhibitor can be divided into parts representing ATP (atoms 1–35), AMP (atoms 36–60) and the bridging phosphate (atoms 61–64) (Fig. 14). In the water simulation, the positional fluctuations of the Ap₅A atoms are of approximately the same size as those of the C $^{\alpha}$ atoms of ADK, except for atoms 18 and 21 of the ATP part and the additional phosphate groups (atoms 60–64), whereas the whole AMP part exhibits significantly larger fluctuations in the in vacuo simulation, too.

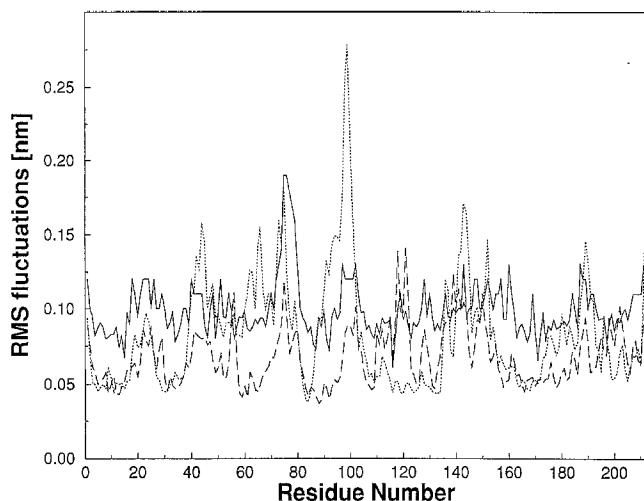


Fig. 12. The positional rms fluctuations of the C $^{\alpha}$ atoms, calculated from the 100–200 ps time-averaged MD structures (dashed line: water; dotted line: vacuum). The positional fluctuations as obtained from the crystallographic B-factors are included for comparison (solid line).

Hydrogen-bonding pattern

Criteria for hydrogen bonding in this study were a maximum distance of 0.25 nm between the hydrogen atom and the acceptor and a minimum angle of 120° between donor–hydrogen–acceptor. This geometrical definition was also used in the analysis of the crystal structure of the ADK complex. The enzyme–inhibitor hydrogen-bonding pattern was analyzed over the complete trajectories of the water and in vacuo simulations and compared to that of the crystal structure. More than 80% of the hydrogen bonds present in the crystal structure were also observed in the water simulation. Structurally important hydrogen bonds, accounting for the binding properties

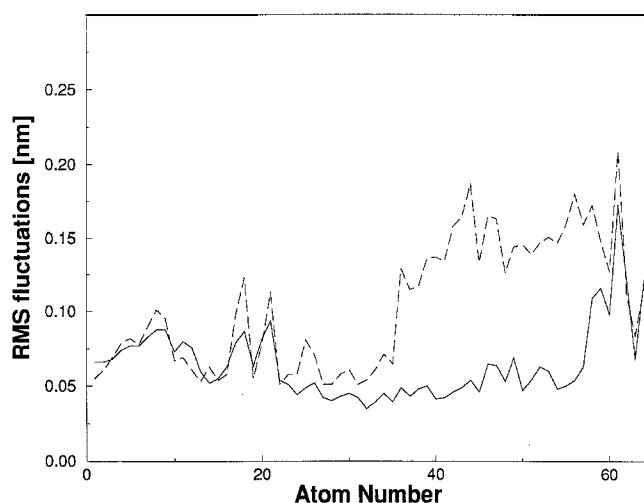


Fig. 13. The positional rms fluctuation of the Ap₅A atoms (ATP part, atoms 1–35; AMP part, atoms 36–62; additional connecting phosphate group, atoms 63–65), obtained from the 100–200 ps water MD time-averaged structure (solid line) and in vacuo averaged structure (dashed line).

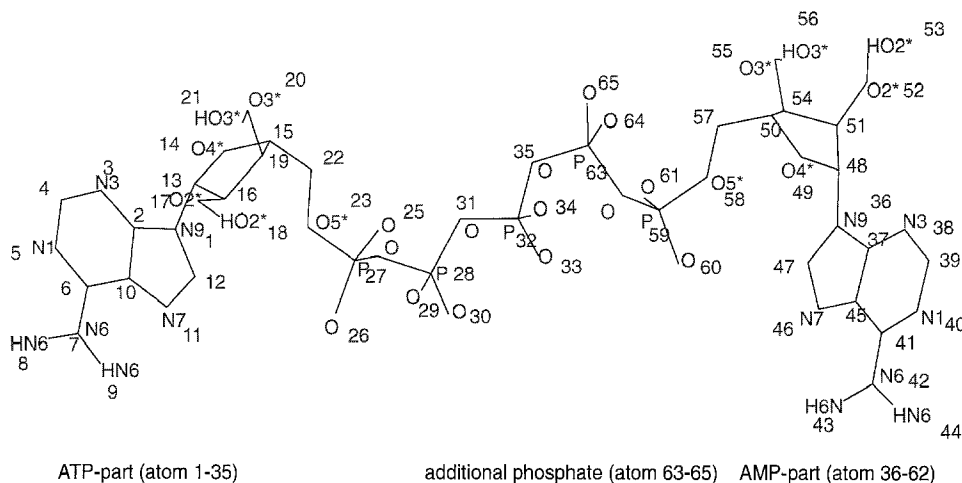


Fig. 14. Crystal structure of the transition-state inhibitor Ap_5A . The left and right sides mimic the ATP part and the AMP part, respectively. All atom types, with the exception of the carbons, are indicated.

of the inhibitor, are well defined in the water simulation. The data of the *in vacuo* simulation again differ considerably from the water simulation and the crystal structure data. Only 30% of the hydrogen bonds in the crystal structure are reproduced, but a large number of new hydrogen-bond pairs appear instead (Table 2).

To determine how accurately the MD simulation reproduces the hydrogen bonds in the crystal structure, the history of the hydrogen bonds observed between the inhibitor and the protein was analyzed and is summarized in Table 3. The residues involved in inhibitor binding can be separated into two classes, ATP- or AMP-binding, and into three further subclasses, adenine-, ribose- and phosphate-binding (Fig. 14). As shown in the crystal structure, ATP is bonded by fewer hydrogen bonds than AMP. Only one hydrogen bond from Lys^{200} to ATP adenine stabilizes the adenine in its binding pocket. However, the adenine HN6 of the ATP part is not permanently bonded to the carbonyl oxygen of Lys^{200} . Every 50 ps the distance between these two atoms becomes larger than 0.3 nm. The fluctuation of this hydrogen bond corresponds with the fluctuation of the ATP part and its positional deviation from the crystal structure. This interaction between the adenine NH_2 -group and Lys^{200} favours ATP over GTP, as proposed by Schulz [10]. Lys^{200} is located in a part of the sequence with low homology to other ADKs, especially AK3, which selectively uses GTP as cosubstrate. Fitting of the backbone of *AKeco* to AK3 results in a good agreement for the central parts of both structures. It has been shown that AMP in AK3 occupies exactly the same position as the AMP part of Ap_5A in *AKeco* [26]. It can be assumed that the cosubstrate (ATP or GTP) binding positions are similar to the other part of Ap_5A . Lys^{201} in AK3, which corresponds to Lys^{200} in *AKeco*, is shifted away from the site of the cosubstrate. Lys^{200} of *AKeco* is located in the loop connecting β -strand 9 and α -helix 8, whereas Lys^{201} in AK3 is already part of the helix following this loop. The distance between the carbonyl group of Lys^{201} and the ATP adenine HN6, which was manually included into the AK3 structure, is larger than 0.9 nm. Hydrogen bonding between these two atoms is impossible at this distance. The stabilization of the ATP adenine by Phe^{137} and Arg^{119} is independent of the base. Either adenine or guanine can be stabilized by formation of a 'sandwich complex'.

TABLE 2
COMPARISON OF HYDROGEN BONDING IN VARIOUS PARTS OF THE ADK-INHIBITOR COMPLEX

COMPARISON OF HYDROGEN BONDS IN VARIOUS STATES OF THE RELEASED ADENINE							
Inhibitor	Residues				X-ray	MD-water 0–300 ps	MD-vacuum 0–200 ps
ATP part							
Adenine	HN6	...	OE	Gln ¹⁶	–	–	+
	HN6	...	O	Lys ²⁰⁰	+	+	–
Ribose	O5'	...	HNH	Arg ¹¹⁹	–	+	+
	O4'	...	HNH	Arg ¹¹⁹	–	+	+
	HO3'	...	O	Tyr ¹³³	+	+	–
	O3'	...	HND	His ¹³⁴	–	+	+
	O3'	...	HN	Phe ¹³⁷	–	–	+
	O2'	...	HN	Asn ¹³⁸	–	–	+
	O3'	...	HN	Val ¹²¹	–	+	–
	HO3'	...	O	Val ¹²¹	–	+	–
α -Phosphate	O	...	HN	Gly ¹²	+	+	–
	O	...	HOG	Thr ¹⁵	+	+	+
	O	...	HN	Thr ¹⁵	+	+	+
β -Phosphate	O	...	HNH	Arg ¹²³	+	+	–
	O	...	HN	Gly ¹⁰	+	+	–
	O	...	HN	Ala ¹¹	+	+	+
	O	...	HN	Gly ¹²	+	+	+
	O	...	HN	Lys ¹³	+	+	–
	O	...	HNZ	Lys ¹³	+	+	–
	O	...	HN	Gly ¹⁴	+	+	+
	O	...	HN	Thr ¹⁵	–	–	+
γ -Phosphate	O	...	HNH	Arg ¹²³	+	+	–
	O	...	HN	Gly ¹⁰	–	+	–
	O	...	HNZ	Lys ¹³	+	+	–
	O	...	HNH	Arg ⁸⁸	–	–	+
	O	...	HNH	Arg ¹²³	+	+	–
	O	...	HNH	Arg ¹⁵⁶	+	–	–
	AMP part						
Adenine	HN6	...	OG	Thr ³¹	+	+	+
	N3	...	HN	Val ⁵⁹	+	+	+
	HN6	...	O	Gly ⁸⁵	+	–	+
	N7	...	HNH	Arg ⁸⁸	–	–	+
	N1	...	HNE	Gln ⁹²	+	+	+
Ribose	O4'	...	HOG	Thr ³¹	–	–	+
	HO2'	...	O	Lys ⁵⁷	+	+	+
	O2'	...	HN	Val ⁵⁹	–	+	+
	N1	...	HN	Thr ⁸⁹	–	–	+
	HO3'	...	OD	Asp ¹⁵⁸	–	–	+
	O5'	...	HNH	Arg ¹⁶⁷	–	–	+
α -Phosphate	O	...	HN	Gly ³²	–	–	+
	O	...	HNH	Arg ³⁶	+	+	–
	O	...	HNH	Arg ⁸⁸	+	–	+
	O	...	HNH	Arg ¹⁵⁶	+	+	–
	Additional phosphate						
phosphate	O	...	HNH	Arg ³⁶	–	–	+
	O	...	HNH	Arg ³⁶	–	–	+
	O	...	HNH	Arg ¹²³	+	+	–
	O	...	HNH	Arg ¹⁵⁶	+	+	–
	O	...	HNH	Arg ¹⁶⁷	+	– (Conf. A)	– (Conf. A)
	O	...	HNE	Arg ¹⁶⁷	+	– (Conf. A)	– (Conf. A)

The hydrogen-bonding pattern was inspected over the whole trajectory and compared with the crystal structure. A hydrogen bond was considered if its occurrence in the simulation was greater than 10%.

TABLE 3
HYDROGEN-BONDING PATTERN OF THE ADK-INHIBITOR COMPLEX

Inhibitor	Residues				Comments
ATP part					
Adenine	HN6	...	O	Lys ²⁰⁰	Unstable, more than 75%
Ribose	O5'	...	HNH	Arg ¹¹⁹	After 40 ps more than 80%
	O4'	...	HNH	Arg ¹¹⁹	Occasionally between 40–300 ps
	O3'	...	HND	His ¹³⁴	~50%, broken after 190 ps, flip of the ring, H-bonded to O2' afterwards
	O3'	...	HN	Val ¹²¹	Occurs only after 210 ps
α -Phosphate	HO3'	...	O	Val ¹²¹	Occurs only after 210 ps
	HO3'	...	O	Tyr ¹³³	Broken after 190 ps, less than 50%
	O	...	HOG	Thr ¹⁵	Permanent after 300 ps
	O	...	HN	Thr ¹⁵	Unstable, stable after 140 ps
β -Phosphate	O	...	HNH	Arg ¹²³	Unstable, ~65%
	O	...	HN	Gly ¹²	Unstable, ~85%
	O	...	HN	Ala ¹¹	More than 90%
	O	...	HN	Gly ¹²	More than 80%
	O	...	HN	Lys ¹³	Fluctuates between two oxygens of the β -phosphate
	O	...	HNZ	Lys ¹³	Permanent fluctuation between all hydrogens of the Lys ¹³ NH ₃ -group
	O	...	HN	Gly ¹⁴	Stable
	O	...	HN	Gly ¹⁰	Broken after 30 ps, fluctuates after 170 ps between different phosphate oxygens
γ -Phosphate	O	...	HNH	Arg ¹²³	Occasionally
	O	...	HN	Gly ¹⁰	Stable
	O	...	HNZ	Lys ¹³	Occasionally; fluctuation between all hydrogens of the Lys ¹³ NH ₃ -group
	O	...	HNH	Arg ¹²³	Between 0 and 160 ps two hydrogen bonds
AMP part					
Adenine	N1	...	HNE	Gln ⁹²	Unstable, occurrence more than 70%
	N3	...	HN	Val ⁵⁹	Unstable, only 25%
	HN6	...	O	Thr ³¹	Broken between 30–60 ps and after 230 ps
Ribose	O2'	...	HN	Val ⁵⁹	Permanent fluctuation, between 0 and 150 ps ~30% and between 150 and 300 ps ~75%
	HO2'	...	O	Lys ⁵⁷	Unstable, more than 80%
α -Phosphate	O	...	HNH	Arg ³⁶	Broken after 50 ps
	O	...	HNH	Arg ¹⁵⁶	Broken after 120 ps
Additional phosphate	O	...	HNE	Arg ¹⁶⁷	Not reproduced, occasionally after 150 ps (other conformation as in the crystal structure)
	O	...	HNE	Arg ¹⁶⁷	Not reproduced, occasionally after 150 ps (other conformation as in the crystal structure)
	O	...	HNH	Arg ¹⁶⁷	Not reproduced, occasionally after 150 ps (other conformation as in the crystal structure)
	O	...	HNH	Arg ¹²³	Nearly permanent, more than 80%, 200–300 ps two hydrogen bonds
	O	...	HNH	Arg ¹⁵⁶	Fluctuates between NH ₂ hydrogens of Arg ¹⁵⁶ , broken after 230 ps

The history of the hydrogen bonds was examined over 300 ps MD in water environment.

Three hydrogen bonds observed between Gln⁹², Val⁵⁹, Thr³¹ and the AMP adenine are relatively stable over the trajectory. These three amino acids are well conserved within the ADK family, explaining the high specificity of adenylate kinases for AMP over GMP [6,13].

Additional hydrogen bonds stabilize both ribose moieties and were inspected during the

simulation. Besides the structural rearrangements within the insertion domain, the Tyr¹³³–ATP ribose hydrogen bond opens after 190 ps. Two new hydrogen bonds appear and connect the ribose to the backbone of Val¹²¹. A change of the His¹³⁴ side-chain hydrogen bond from O3' to O2' of the ATP ribose can be observed at 190 ps, due to a 180° rotation of the imidazole ring. The parallel orientation of the Arg¹¹⁹ side chain to the ATP adenine moiety results in two additional hydrogen bonds to the ribose. Either ribose or deoxyribose are accepted as sugar moieties from *AKeco* [25]. The O2' oxygen of the ribose, which is absent in deoxyribose, is only very occasionally hydrogen bonded to the surrounding amino acids.

The high density of positively charged arginine and lysine residues around the negatively charged pentaphosphate is responsible for the tight binding of the phosphate groups. The positively charged guanidinium groups of the arginine residues around Ap₅A adopt a parallel staggered conformation after a few picoseconds of MD simulation. The α -phosphate of the AMP part and the additional connecting phosphate group have fewer positively charged residues in their neighbourhood. This observation corresponds to the larger positional flexibility of these two phosphate groups. A contact between Arg¹⁶⁷ HNH and the connecting phosphate group, as seen in conformation B in the crystal structure, was not observed during the MD simulation. The side chain of Arg¹⁶⁷ does not contact any phosphate group in conformation A, which was used in our study. A reorientation of the guanidinium group towards a phosphate group is not observed. However, a hydrogen bond between Arg¹⁶⁷ and the phosphate oxygen occurs occasionally after 150 ps.

The side chain of the highly conserved Asp¹⁵⁸ residue, which fixes the guanidinium groups of Arg¹⁵⁶ in the crystal structure, rotates and points away from this arginine during the simulation. The loss of this salt bridge is followed by an opening of the hydrogen bond between the Arg¹⁵⁶ HNH and the α -phosphate of the AMP part at 170 ps, which can then change its location and conformation. The interaction between the α -phosphate and Arg⁸⁸ is not observed during the MD simulation. The guanidinium side chain has rotated and moved away from its crystal position. Arg⁸⁸ then folds around the AMP adenine NH₂-group and faces the phosphate-binding loop of the protein. The hydrogen bond between the Arg¹⁵⁶ side chain and the γ -phosphate oxygen cannot be reproduced during the simulation. Lys¹³ lies on one side of the γ -phosphate group and the Arg¹⁵⁶ guanidinium group faces the γ -phosphate from the opposite side. However, the guanidinium group of Arg¹⁵⁶ fixes the additional phosphate group and the α -phosphate of the AMP part.

Lys¹³ of *Akeco*, or an analogous lysine residue in homologous proteins, located in the phosphate-binding loop, is proposed to be responsible for defining the exact position of the phosphates in the loop in all nucleotide-binding proteins. It may also play a catalytic role. During the catalyzed reaction, the γ -phosphate of ATP is transferred to AMP. It was assumed that the Lys¹³ side chain should remain attached to the γ -phosphate over the whole transfer path [10]. Nevertheless, this hydrogen bond occurs only occasionally. On the other hand, the Lys¹³ side chain is strongly connected to the β -phosphate. Compared to other side chains as those of Phe¹³⁷ or His¹³⁴, Lys¹³, which is not fully extended, maintains a stable conformation during the simulation. Only a small movement away from the γ -phosphate could be observed, so that hydrogen bonding was not possible anymore. However, the importance of Lys¹³ was already demonstrated by the point mutation K13Q, which resulted in an increase of the K_m of both substrates ATP and AMP, comparable to all other point mutations in the P-loop [27]. The analogous lysine residues of Ef-Tu and H *ras*-p21 also encircle the β -phosphate group, which agrees with our observation during the MD simulation [28,29].

Catalysis and Mg^{2+} binding

Phosphotransferases and a number of other proteins with different functions require a divalent cation complexed to a phosphoryl group for their catalytic activity. Examples of such proteins are phosphokinases, guanylate kinases and adenylate kinases. The general features of the Mg^{2+} - and phosphoryl-binding domains are apparent, even in the nucleotide-binding fold of a more divergent structure such as the rec A protein [30].

The presence of an Mg^{2+} ion is essential to weaken the β - γ -phosphate bond or to activate the nucleophile. The GTPase activity of EF-Tu and H *ras*-p21 is dependent on the complexation with an Mg^{2+} ion [28,29]. Comparisons of either kinases or guanine nucleotide-binding proteins exhibit similarities in the coordination of the cation: Mg^{2+} always adopts an octahedral coordination geometry and often one or two phosphate groups act as ligands. Crystal structures with well-defined Mg^{2+} -binding sites are only available for PFK, H *ras*-p21 and Ef-Tu [28,29,31].

Nucleotide-binding proteins share common structural motifs, such as the P-loop, the $\beta\alpha\beta$ -fold and the central β -sheet. The P-loop fixes the γ -phosphate and enables it to be attacked by a nucleophile. Important residues involved in nucleotide binding or Mg^{2+} coordination lie at the ends of β -strands or within the loops immediately following the β -strands. These residues, involved in binding of Mg^{2+} , prefer β -strands which are adjacent or in the neighbourhood of the P-loop. In most cases Mg^{2+} is complexed to three negatively charged ligands and three uncharged oxygen ligands. Either serine or threonine side chains of highly conserved residues, phosphate oxygen atoms or carboxyl groups of aspartic acid residues are suitable ligands for Mg^{2+} coordination. The Mg^{2+} coordination takes place either directly or mediated by water molecules.

As an Mg^{2+} ion could not be determined in the crystal structure of the ADK from *E. coli*, the ligands can only be predicted from simulation results. The assignment of possible amino acids for Mg^{2+} complexes is first made from the secondary structure. Three aspartic acid residues within the structure lie at the end of β -strands neighbouring the central P-loop: Asp⁸⁴ at the end of β -strand 3, Asp¹¹⁰ at the end of β -strand 4 and Asp³³ at the beginning of α -helix 2. Suitable serine- and threonine residues can only be found at positions Ser³⁰, Thr³¹ and Thr⁸⁹. The Thr³¹ side chain points towards the AMP part in the active site and forms a hydrogen bond to the AMP adenine. Distance measurements between the phosphate groups and aspartic acid, serine and threonine side chains showed that an Mg^{2+} ion would have enough space in between to be complexed by these residues.

Additional calculations with the GRID program [32] were carried out in order to define the positions in the active site at which a positively charged Mg^{2+} ion would interact favourably. The complete protein-inhibitor complex was reduced to its active site, including 60 residues within 0.7 nm around Ap₅A. All calculations were done with an Mg^{2+} as the probe atom and with a grid size of 0.05 nm. From the crystal structure and both average structures of the water simulation, it followed that the most suitable location for the Mg^{2+} ion would be near the β - and γ -phosphate groups, facing the Asp³³ and Asp⁸⁴ residues (Fig. 15).

The carboxyl group of Asp⁸⁴ moved closer to the γ -phosphate group during the simulation. The distance decreased from 0.6 to 0.45 nm, which is appropriate for Mg^{2+} binding. However, the Asp³³ and Asp¹¹⁰ side chains are more than 1.0 nm away, making a correct coordination geometry impossible. Furthermore, the Ser³⁰ hydroxyl group, approximately 0.6 nm away, can act as an additional Mg^{2+} ligand, possibly supported by a water molecule. However, the presence of a positively charged Mg^{2+} could attract the negative side chains of the aspartic acid residues or

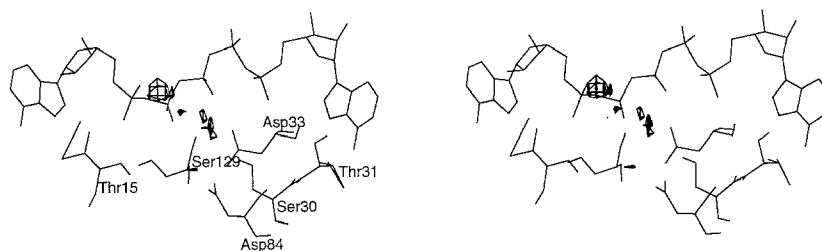


Fig. 15. The crystal structure of Ap₅A and surrounding residues. The contours indicate the most suitable location for the Mg²⁺ ion between the β- and the γ-phosphate groups, as calculated by the GRID program [32].

the electronegative oxygen of Ser³⁰ and thus lead to shorter distances that are more favourable for complexation. Aside from the phosphate groups and the aspartic acid and serine residues, the coordination can also be completed by water molecules, as has been shown in the Ef-Tu and ras p21 structures [28,29]. The difference in binding affinity for Ap₅A in the presence and absence of Mg²⁺ is higher for the K13Q mutant than for the wild type. In the absence of a Lys¹³ side chain, which seems to be necessary for the correct Ap₅A binding, Mg²⁺ could take over its functions.

CONCLUSIONS

The MD simulation of the AK_{eco}-Ap₅A enzyme complex for 300 ps in water environment is able to properly explain biochemical data. As shown earlier, a corresponding simulation in vacuo does not give reliable results, although the GROMOS parameters have been adapted to account for the vacuum boundary conditions. Explicit inclusion of water molecules in the simulation is essential to obtain an accurate model. The exclusion of all water molecules from the active site, especially from the phosphate groups, is not satisfactory because several water molecules are hydrogen-bonded to the γ-phosphate group, thus interacting as nucleophilic partners for an attack on this phosphate group.

The enzyme consists of separate domains, which can change their location relative to each other during the catalysis reaction. Dynamical motions of the insertion domain reveal the importance of this domain for the enzyme reaction. Structural change in this domain affects other parts of the protein more than in the main and AMP-binding domains. Although AK_{eco}, crystallized with Ap₅A, resembles the 'final state' of the enzyme reaction at which the insertion domain should remain closed, its hinge regions can still be localized during the simulation.

The protein structure, as obtained from trajectory averages of the water simulation, agrees well with the crystal structure. The selectivity for the substrate and the variability in the cosubstrate part can be explained by data of the present simulation. The hydrogen-bonding data of Lys¹³ do not support the hypothesis that this residue is essential for the γ-phosphate transfer.

ACKNOWLEDGEMENTS

We thank Prof. G. Schulz for providing the crystallographic coordinates in advance of release to the Brookhaven Data Bank and Prof. W.F. van Gunsteren for helpful discussions.

REFERENCES

- 1 Schulz, G.E., *Curr. Opin. Struct. Biol.*, 2 (1992) 61.
- 2 Baker, P.J., Britton, K.L., Rice, D.W., Rob, A. and Stillman, T.J., *J. Mol. Biol.*, 228 (1992) 662.
- 3 Elion, G.B., Furman, P.A., Fyfe, J.A., DeMiranda, P., Beauchamp, L. and Schaeffer, H.J., *Proc. Natl. Acad. Sci. USA*, 74 (1977) 5716.
- 4 Munch-Petersen, B. and Tyrsted, G., *Leuk. Res.*, 12 (1988) 173.
- 5 Follers, G., Trumpp-Kallmeyer, S., Gutbrod, O., Krickl, S., Fetzter, J. and Keil, G.M., *J. Comput.-Aided Mol. Design*, 5 (1991) 385.
- 6 Schulz, G.E., Schiltz, E., Tomaselli, A.G., Frank, R., Brune, M., Wittinghofer, A. and Schirmer, R.H., *Eur. J. Biochem.*, 161 (1986) 127.
- 7 Diederichs, K. and Schulz, G.E., *Biochemistry*, 29 (1990) 8138.
- 8 Tsai, M.-D. and Yan, H., *Biochemistry*, 30 (1991) 6806.
- 9 Liang, P., Phillips Jr., G.N. and Glaser, M., *Proteins*, 9 (1991) 28.
- 10 Müller, C.W. and Schulz, G.E., *J. Mol. Biol.*, 224 (1992) 159.
- 11 Saraste, M., Sibbald, P.R. and Wittinghofer, A., *Trends Biochem. Sci.*, 15 (1990) 430.
- 12 Schulz, G.E., Müller, C.W. and Diederichs, K., *J. Mol. Biol.*, 213 (1990) 627.
- 13 Holmes, R.K. and Singer, M.F., *J. Biol. Chem.*, 248 (1973) 2014.
- 14 Van Gunsteren, W.F. and Berendsen, H.J.C., *Groningen Molecular Simulation (GROMOS) Library Manual*, Biomos, Groningen, 1987.
- 15 SYBYL 6.0, Tripos Associates, Inc., St. Louis, MO.
- 16 Berendsen, H.J.C., Grigera, J.R. and Straatsma, T.P., *J. Phys. Chem.*, 91 (1987) 6269.
- 17 Ryckaert, J.P., Cicotti, G. and Berendsen, H.J.C., *J. Comput. Phys.*, 23 (1977) 327.
- 18 Berendsen, H.J.C., Postma, J.P.M., Van Gunsteren, W.F., DiNola, A. and Haak, J.R., *J. Chem. Phys.*, 81 (1984) 3684.
- 19 Levitt, M. and Sharon, R., *Proc. Natl. Acad. Sci. USA*, 85 (1988) 7557.
- 20 Harte, W.E., Swaminathan, S. and Beveridge, D.L., *Proteins*, 13 (1992) 175.
- 21 Foley, C.K., Pedersen, L.G., Charifson, P.S., Darden, T.A., Wittinghofer, A., Pai, E.F. and Anderson, M.W., *Biochemistry*, 31 (1992) 4951.
- 22 Kabsch, W. and Sander, C., *Biopolymers*, 22 (1983) 2577.
- 23 Schulz, G.E., *Curr. Opin. Struct. Biol.*, 2 (1992) 61.
- 24 Gerstein, M., Schulz, G. and Chotia, C., *J. Mol. Biol.*, 229 (1993) 494.
- 25 Saint-Girons, I., Gilles, A., Margarita, D., Michelson, S., Monnot, M., Fermandjian, S., Danchin, A. and Barzu, O., *J. Biol. Chem.*, 262 (1987) 622.
- 26 Schulz, G.E., Müller, C.W. and Diederichs, K., *J. Mol. Biol.*, 213 (1990) 627.
- 27 Reinstein, J., Schlichting, I. and Wittinghofer, A., *Biochemistry*, 29 (1990) 7451.
- 28 Pai, E.F., Kregel, U., Petsko, G.A., Goody, R.S., Kabsch, W. and Wittinghofer, A., *EMBO J.*, 9 (1990) 2351.
- 29 Kjeldgaard, M. and Nyborg, J., *J. Mol. Biol.*, 223 (1992) 721.
- 30 Story, R.M. and Steitz, T.A., *Nature*, 355 (1992) 374.
- 31 Shirakihara, Y. and Evans, P.R., *J. Mol. Biol.*, 204 (1988) 973.
- 32 Goodford, P.J., *J. Med. Chem.*, 28 (1985) 849.